Acta Crystallographica Section D
Biological Crystallography
ISSN 0907-4449

X-ray structure of the metcyano form of dehaloperoxidase from *Amphitrite ornata*: evidence for photoreductive dissociation of the iron–cyanide bond

V. S. de Serrano,[a] M. F. Davis,[a] J. F. Gaff,[a] Qi Zhang,[a] Z. Chen,[a] E. L. D'Antonio,[a] E. F. Bowden,[a] R. Rose[b] and S. Franzen[a]*

[a]Department of Chemistry, North Carolina State University, Raleigh, NC 27695, USA, and [b]Department of Biochemistry, North Carolina State University, Raleigh, NC 27695, USA

Correspondence e-mail: stefan_franzen@ncsu.edu

Received 27 January 2010
Accepted 20 April 2010

PDB References: metcyano form of dehaloperoxidase, wild type, 3kun; C73S mutant, 3kuo.

X-ray crystal structures of the metcyano form of dehaloperoxidase-hemoglobin (DHP A) from *Amphitrite ornata* (DHPCN) and the C73S mutant of DHP A (C73SCN) were determined using synchrotron radiation in order to further investigate the geometry of diatomic ligands coordinated to the heme iron. The DHPCN structure was also determined using a rotating-anode source. The structures show evidence of photoreduction of the iron accompanied by dissociation of bound cyanide ion (CN^-) that depend on the intensity of the X-ray radiation and the exposure time. The electron density is consistent with diatomic molecules located in two sites in the distal pocket of DHPCN. However, the identities of the diatomic ligands at these two sites are not uniquely determined by the electron-density map. Consequently, density functional theory calculations were conducted in order to determine whether the bond lengths, angles and dissociation energies are consistent with bound CN^- or O_2 in the iron-bound site. In addition, molecular-dynamics simulations were carried out in order to determine whether the dynamics are consistent with trapped CN^- or O_2 in the second site of the distal pocket. Based on these calculations and comparison with a previously determined X-ray crystal structure of the C73S–O_2 form of DHP [de Serrano *et al.* (2007), *Acta Cryst.* D**63**, 1094–1101], it is concluded that CN^- is gradually replaced by O_2 as crystalline DHP is photoreduced at 100 K. The ease of photoreduction of DHP A is consistent with the reduction potential, but suggests an alternative activation mechanism for DHP A compared with other peroxidases, which typically have reduction potentials that are 0.5 V more negative. The lability of CN^- at 100 K suggests that the distal pocket of DHP A has greater flexibility than most other hemoglobins.

1. Introduction

Dehaloperoxidase (DHP A) is a truncated hemoglobin originally isolated from the terebellid polychaete *Amphitrite ornata* that has been cloned and expressed in *Escherichia coli* (Belyea *et al.*, 2005). DHP A is unique within the globin family because it is bifunctional, with both O_2-transport and peroxidase activities, which are regulated by external substrate binding and internal inhibitor binding (Thompson *et al.*, 2010). Two genes code for dehaloperoxidase-hemoglobins in *A. ornata*: *dhpA* and *dhpB* (Han *et al.*, 2001). We have recently cloned the protein product of the second gene, DHP B, which has a higher peroxidase activity than DHP A (de Serrano *et al.*,

2010). In this study, we continue our investigation of the ligand-binding properties of DHP A by determining cyanide-adduct structures under conditions where photoreduction may be taking place. The activity of peroxidases is related to the reduction potential of the active-site Fe. For O_2 transport, globins maintain the ferrous Fe^{II} state, while the resting state for peroxidases is the ferric Fe^{III} state. Photoreduction of ferric heme proteins is often observed in the high flux of synchrotron radiation. Here, we have compared the use of high-flux and low-flux X-ray sources combined with molecular modeling in order to understand the effect of Fe reduction on the active-site ligation and structure.

DHP A catalyzes the oxidative dehalogenation of 2,4,6-trihalophenols, according to Fig. 1, leading to the formation of the corresponding 2,4-dihaloquinones (Chen *et al.*, 1996; Belyea *et al.*, 2005, 2006; Franzen *et al.*, 2007; Feducia *et al.*, 2009). The dehaloperoxidase reactivity of DHP A shown in Fig. 1 is believed to be an important function in *A. ornata* (Chen *et al.*, 1996; Lincoln *et al.*, 2005), in addition to the oxygen-transport function that is common to hemoglobins (Hbs). Despite the apparent simplicity of the globin structure, the structure–function relationships of DHP A have only begun to be elucidated. The mutually exclusive binding of inhibitor and substrate to DHP has recently been studied by NMR and X-ray crystallography (Davis *et al.*, 2009; Thompson *et al.*, 2010).

The X-ray crystal structures of the metaquo (PDB code 2qfk), oxy (PDB code 2qfn) and deoxy (PDB code 3dr9) forms of DHP show that there is a correlation between the position of the distal histidine His55 and the coordination state of the heme iron (de Serrano *et al.*, 2007; Chen *et al.*, 2009). In five-coordinate high-spin (5cHS) adducts His55 is observed in a solvent-exposed or open conformation, as in the 100 K deoxy structure (PDB code 3dr9). However, in six-coordinate high-spin (6cHS) adducts His55 is in an internal or closed conformation in hydrogen-bonding contact with heme-bound H_2O or O_2 (PDB codes 2qfk and 2qfn, respectively). Complete understanding of the binding to the heme iron requires further study of the dependence of the histidine conformation on the coordination state of the heme iron.

The CN^- adduct is a useful probe of the active-site geometry of heme-containing enzymes and oxygen carriers (Bolognesi *et al.*, 1999; Edwards & Poulos, 1990; Fukuyama & Okada, 2007; Fedorov *et al.*, 2003; Furtmüller *et al.*, 2006; Sugishima *et al.*, 2003). CN^- binds to the ferric form of heme proteins and inhibits both enzymatic activity and oxygen transport (Chance, 1943). The metcyano form of DHP has proven to be useful for solution structural studies using ^1H hyperfine NMR spectroscopy, which have probed the interactions of halogenated phenols with the protein in solution (Davis *et al.*, 2009). The X-ray crystal structures of the CN^- adducts of many heme proteins have provided detailed insight into the interaction of the diatomic ligand with the amino-acid side chains in the distal pocket. Although model systems have an Fe—C—N angle of nearly 180°, there are examples of smaller Fe—C—N angles that are caused by interaction with the amino acids in the distal cavity (Sugishima *et al.*, 2003). CN^- and H_2O_2 have similar binding dependencies. For example, in human myeloperoxidase it was postulated that CN^- provides a model for the intermediate Compound I (Blair-Johnson *et al.*, 2001).

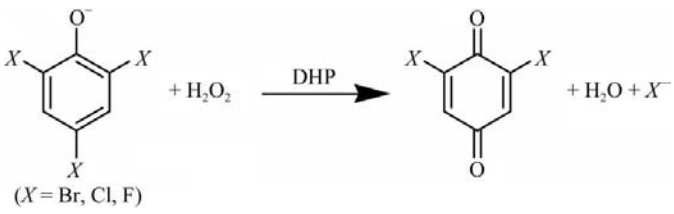

Figure 1
Oxidative dehalogenation of 2,4,6-trihalophenols catalyzed by DHPA.

Hemoglobins and myoglobins have provided unique information on the dynamics of diatomic ligands as they move through the protein on their way to or from the heme iron. The carbonmonoxy adduct DHPCO is isoelectronic with the metcyano adduct DHPCN, providing comparisons by using Fourier transform infrared (FTIR) spectroscopy to determine the effects of amino-acid interactions with the heme-iron-bound CO. We are particularly interested in understanding the relationship between DHPCN and metcyano myoglobin (MbCN) in order to elucidate the significance of the CO trajectories in both proteins that have been measured using temperature-derivative spectroscopy (TDS; Nienhaus *et al.*, 2006, 2008). Hence, the questions addressed by an X-ray structure of DHPCN pertain not only to the binding of CN^- but also to the protein dynamics that accompany ligand photodissociation. The observed electron density in the distal pocket indicates a ligand trajectory since there is density at a site not coordinated to the heme iron. This observation may be important in a dual-function protein that binds both O_2 and H_2O_2 in a manner that requires ligand exchange for function.

Here, we report that the CN^- ligand dissociates from the heme iron of DHPCN during the X-ray experiment owing to photoreduction of the iron from the ferric to the ferrous state. We have compared the structural results obtained using synchrotron radiation with those from a rotating-anode X-ray source, both of which show evidence that the Fe—CN bond is broken during the course of data collection at 100 K. The significance of this comparison is that we have attempted to determine the effect of the radiation dose on the yield of photoreduction of Fe^{III} to Fe^{II}. The crystals studied were approximately 100 µm in each dimension, which permits the absorbed doses to be estimated as 7×10^6 and 0.3×10^6 Gy (where 1 Gy = 1 J kg^{-1}) for the synchrotron and in-house rotating-anode sources, respectively. To obtain these values, the appropriate fluxes for each source were used (see §2) and the assumption was made that 2% of the incident X-ray flux was absorbed by the crystal (Murray *et al.*, 2005). Although the doses differ by a factor of ∼20, the flux is ∼380 times larger for synchrotron radiation. In order to avoid beam damage, the typical synchrotron exposure times used were 19 times shorter than those for the rotating-anode source. Photoreduction and photolysis of a ligand can depend strongly on the flux. As a

result of the greater flux and perhaps also the total dose, both photoreduction of metcyano heme proteins and photolysis of ligands are observed (Keilin & Hartree, 1955); the photoreduction phenomenon has been observed previously during structure determination of heme proteins using synchrotron radiation (Chance *et al.*, 1980; George *et al.*, 2008).

Accordingly, in a previous study we found that *in situ* photoreduction of Fe^{III} in the C73S mutant of DHP by the X-ray beam leads to the binding of O_2 to the heme iron (de Serrano *et al.*, 2007). The C73S mutant was originally investigated in order to eliminate the possibility of reactions involving the surface cysteine Cys73. In the present study, the diatomic ligand in both the C73S (C73SCN) and wild-type (DHPCN) structures resides in two positions in the distal pocket whose relative populations appear to depend on the X-ray beam exposure. However, the fact that the initial ligand is CN^- required more extensive study in order to explain the fate of the photoreduction and dissociation processes in the DHPCN and C73SCN crystals at 100 K. Because of the difficulties in making a definitive assignment of the electron density in the distal pocket, we have studied the bonding and protein dynamics associated with this process using both density functional theory (DFT) calculations and molecular-dynamics (MD) simulations. The combination of calculations and experimental data elucidate the factors that govern the loss of the CN^- ligand during X-ray exposure in these crystal structures. The trajectory of CN^- provides insight into the motions of O_2 and H_2O_2 in the distal pocket, which are key determinants of function in DHP A.

2. Materials and methods

2.1. Preparation of crystals of CN^--bound complexes

Wild-type DHP and C73S mutant protein were expressed in Rosetta(DE3)pLysS cells (Novagen, Madison, Wisconsin, USA) and purified as described previously (de Serrano *et al.*, 2007). DHPCN complexes were prepared by incubating 8 mg ml^{-1} protein in 20 m*M* sodium cacodylate buffer pH 6.5 with 10 m*M* KCN for 30 min on ice prior to crystallization setup. The crystallization conditions were similar to those described for DHP in the absence of any added ligands (de Serrano *et al.*, 2007). Crystals were grown by the hanging-drop vapor-diffusion method, with reservoir solution containing unbuffered 0.2 *M* ammonium sulfate and PEG 4000 at a concentration in the range 28–34%(*w*/*v*). Diffraction-quality crystals grew within one week at 277 K.

2.2. Data collection, processing and refinement

Diffraction data were collected at 100 K on the SER-CAT 22-BM beamline at the Advanced Photon Source (Argonne, Illinois, USA) using an X-ray wavelength of 1.0 Å. Both DHPCN and C73SCN crystals diffracted to 1.26 Å resolution on a MAR 225 detector. A data set for DHPCN was also collected on a Rigaku MicroMax-007 HF copper rotating-anode X-ray generator (λ = 1.54 Å). The DHPCN crystal diffracted to 1.72 Å resolution on an R-AXIS IV^{++} image-plate detector. The 22-BM beamline, with a photon flux of 3×10^{13} photons s^{-1} mm^{-2} and an average exposure of 5 s per frame (120 frames in total) at an energy of 12 keV (λ = 1 Å), delivers an X-ray dose to a crystal that is approximately an order of magnitude larger than an in-house Micromax-007 HF Cu rotating-anode X-ray generator with a flux of 7.8×10^{10} photons s^{-1} mm^{-2} and 180 s exposure per frame (90 frames in total) at an energy of 8 keV (λ = 1.54 Å).

The diffraction data were processed using *DENZO* and *SCALEPACK* (Otwinowski & Minor, 1997). The CN-complex crystals belonged to the primitive orthorhombic space group $P2_12_12_1$, analogous to C73S mutant and wild-type protein crystals that do not contain added ligand, and have very similar unit-cell parameters: $a = 57.2$, $b = 66.6$, $c = 68.7$ Å for the wild-type complex and $a = 57.7$, $b = 66.5$, $c = 68.2$ Å for the C73S mutant complex, respectively (de Serrano *et al.*, 2007). The 1.62 Å resolution structure of metaquo DHP determined at 100 K was used as the starting model for molecular replacement with *Phaser* (McCoy *et al.*, 2005) and subsequent refinement steps were carried out using the *CCP*4 suite of programs (Collaborative Computational Project, Number 4, 1994). In the refinement procedures, model bias was eliminated by constructing OMIT maps with the *CNS* program (Brünger *et al.*, 1998), omitting the relevant residues or heme-bound ligand from the map calculations. With the resolution of 1.26 Å for each crystal form, we were able to model approximately one third of the residues in each subunit of each structure in two conformations. Notably, the distal histidine residue (His55) was modeled in two conformations within the distal pocket, as were the aromatic residues defining the distal pocket hydrophobic cavity. The alternative occupancies of the ligand were defined by the appearance of a second alternative conformation of CN^- in the distal pocket during acquisition of the X-ray diffraction data set. These conformations of CN^- may in fact be a consequence of O_2 entering the distal pocket following photoreduction of Fe^{III}. This hypothesis was examined using model calculations. Furthermore, in order to evaluate the effect of X-ray exposure on the development of the electron density attributed to the alternative CN^- conformation, we have grouped and scaled the collected data set to include only a set of the first and/or last collected diffraction images of the data set.

Final models were obtained by iterative cycles of model building in *Coot* (Emsley & Cowtan, 2004) using $2F_o - F_c$ (contoured at the 1σ level) and $F_o - F_c$ (contoured at the 3σ level) electron-density maps and positional and anisotropic *B*-factor structure refinement using *REFMAC*5 (Murshudov *et al.*, 1997) from the *CCP*4 suite of programs (Collaborative Computational Project, Number 4, 1994) and *CNS* (Brünger *et al.*, 1998). Simulated-annealing and composite OMIT maps were constructed with the *CNS* program. Structural figures were prepared using *PyMOL* (DeLano, 2002).

The final models of the DHPCN and C73SCN structures refined to R/R_{free} values of 15.7/18.7% and 17.7/19.8%, respectively, for the synchrotron-radiation data sets. The models contained two polypeptide chains, two CN^- ions, two sulfate ions and 352 or 324 water molecules for DHPCN and

Table 1
Data-collection and refinement statistics.

Values in parentheses are for the highest resolution shell. The sixth coordination ligand of heme Fe is a CN^- ion; data are compiled for the first 90 diffraction images (of the 120 collected) for the data sets obtained at the synchrotron.

	Wild-type, recombinant, CN complex	C73S mutant, CN complex	Wild-type, recombinant, CN complex
PDB code	3kun	3kuo	
Source	Synchrotron	Synchrotron	Rotating anode
Data collection			
Wavelength (Å)	1.0	1.0	1.5418
Space group	$P2_12_12_1$	$P2_12_12_1$	$P2_12_12_1$
Unit-cell parameters			
a (Å)	57.2	57.7	58.8
b (Å)	66.6	66.5	67.7
c (Å)	68.7	68.2	67.7
Resolution (Å)	35.0–1.26 (1.29–1.26)	35.0–1.26 (1.29–1.26)	37.1–1.72 (1.77–1.72)
Unique reflections	67355 (4633)	66582 (4665)	27852 (2037)
Completeness (%)	97.2 (96.5)	96.3 (94.8)	99.3 (100.0)
R_{merge}† (%)	5.3 (32.4)	5.2 (53.6)	5.7 (53.2)
$I/\sigma(I)$	21.9 (2.6)	25.4 (2.0)	26.3 (2.3)
Redundancy	3.5 (3.3)	3.3 (2.9)	3.4 (3.3)
Refinement			
R_{work}‡ (%)	15.7	17.6	18.8
R_{free}§ (%)	18.7	19.8	23.0
Average *B* factor (Å^2)			
All atoms	12.0	13.4	18.0
Protein	10.4	12.0	17.3
Water	24.2	25.1	25.6
No. of protein atoms	2896	2966	2815
No. of solvent atoms	352	324	255
R.m.s.d. from ideal geometry			
Bond lengths (Å)	0.006	0.007	0.008
Bond angles (°)	1.02	1.08	1.11
Ramachandran plot¶ (%)			
Most favored region	94.8	94.8	95.2
Additional allowed region	5.2	5.2	4.8

† $R_{merge} = \sum_{hkl}\sum_i |I_i(hkl) - \langle I(hkl)\rangle| / \sum_{hkl}\sum_i I_i(hkl)$, where $I_i(hkl)$ is the *i*th measurement and $\langle I(hkl)\rangle$ is the weighted mean of all measurements of $I(hkl)$. ‡ $R_{work} = \sum_{hkl} ||F_{obs}| - |F_{calc}|| / \sum_{hkl} |F_{obs}|$, where F_{obs} are the observed and F_{calc} are the calculated structure factors. § R_{free} is the *R* factor for a subset (5%) of reflections selected before and not included in refinement. ¶ Calculated using *PROCHECK* (Laskowski *et al.*, 1993).

C73SCN, respectively. The data-collection and model statistics for the X-ray data sets are summarized in Table 1.

2.3. Binding-constant determination

KCN titrations were conducted in 50 m*M* phosphate buffer pH 6.5 and 100 m*M* NaCl. The pH was chosen to be the same as that of the crystallization buffer. The binding constants were measured at ambient temperature. Titrations were performed in a cuvette in a Hewlett–Packard 8453 diode-array spectrophotometer. Changes in the absorbance at the wavelength of the Soret maximum were measured and converted into relative populations of the cyanide and metaquo forms as described elsewhere (Thompson *et al.*, 2010).

2.4. Spectroelectrochemical determination of formal reduction potentials

Spectroelectrochemistry (SEC) experiments were carried out in 100 m*M* potassium phosphate buffer at pH 7.00 ± 0.02 in an air-tight UV–visible cell that utilized an optically transparent thin-layer electrode, namely indium–tin oxide (ITO). The ITO electrode was thoroughly cleaned before use by 10 min successive sonications in 1%(*v*/*v*) Contrex solution (Decon Labs Inc.), 95% ethanol and twice in deionized water. The SEC cell was stored in a nitrogen-atmosphere drybox for at least 8 h prior to experimentation. UV–visible spectra were recorded using a Hewlett–Packard 8453 spectrophotometer and the applied potentials were controlled with a Model 273A Princeton Applied Research potentiostat. The SEC cell made use of an Ag/AgCl (saturated KCl) reference electrode (Microelectrodes Inc.) and a platinum-wire auxiliary electrode (Alfa Aesar). The reduction potential of C73S-DHP is referenced to the standard hydrogen electrode (SHE). The electron-transfer mediators tetramethyl *p*-phenylenediamine (TMPD; Sigma) and tris (ethylenediamine)ruthenium(II) tetrachlorozincate, $[Ru(en)_3]^{2+}$, which we synthesized using a previously described procedure (Smolenaers & Beattie, 1979), were used to facilitate electron transfer between DHP and the electrode. The ratio of DHP to mediators was 2:1.

2.5. Density functional theory (DFT) calculation of potential energy surfaces

DFT calculations of the potential energy surfaces were used to model the bond strength and possible dissociation of the cyanide from different spin and oxidation states of the iron. Geometry optimizations were performed for heme in the low-spin state for both ferric and ferrous oxidation states with either the O_2 or CN^- ligand. All calculations were implemented using the electronic structure package *DMol*^{3} (Delley, 1990, 2000). The generalized gradient approximation of the BLYP (Becke, 1988; Lee *et al.*, 1988) density functional is utilized in the ground-state energy calculation, using a double numeric basis set with one polarization function. Optimized geometries were obtained using the conjugate-gradient method constrained to an energy difference of 10^{-6} Hartrees (1 Hartree = 27.2 eV). Potential energy surfaces were calculated implementing the thermal treatment (Weinert & Davenport, 1992) of the density functional. The grand canonical calculation was carried out at a finite temperature of 0.02 Hartrees. The system used to model the heme in geometry optimizations consists of an imidazole bound to the central iron in porphine (FeP), with both CN^- and O_2 ligands initially bound *trans* to the imidazole.

2.6. Molecular-dynamics (MD) simulations

MD simulations were employed in order to determine the trajectory of the dissociated ligand for comparison with the

Table 2
Comparison of heme iron and ligand distances for metcyano adducts.

The values are tabulated for subunit *A* of the asymmetric unit.

Protein form	Wild type†	C73S†	Wild type‡	
Source	Synchrotron	Synchrotron	Rotating anode	
			Chain *A*	Chain *B*
Fe—His89 $N^{\varepsilon 2}$ (Å)	2.17	2.13	2.16	2.15
Fe—His55*a*§ $N^{\varepsilon 2}$ (Å)	5.01	5.02	5.43	5.62
Fe—His55*b*§ $N^{\varepsilon 2}$ (Å)	5.38	5.32	5.23	5.08
Fe—His55*c* ND1 (Å)	—	—	8.19	7.92
Outside distal pocket				
Fe–ligand¶ (CN1) (Å)	2.05	2.16	2.29	2.19
Fe–ligand¶ (CN2) (Å)	3.11	3.20	—	—
Ligand–His55††				
CN1 N—His55*a* $N^{\varepsilon 2}$ (Å)	3.40	3.56	2.82	3.38
CN2 N—His55*a* $N^{\varepsilon 2}$ (Å)	2.84	2.87	—	—
Fe–pyrrole N plane (Å)	0.05	0.05	0.08	0.1
Fe–ligand bend angle‡‡ (°)				
CN1	125	117§§	154	127
CN2	175	158		
Fe–ligand tilt angle¶¶ (°)				
CN1	6	7	11	14
CN2	14	19		

† Structures of wild-type recombinant and C73S mutant protein in complex with cyanide ion. ‡ Values for both chains *A* and *B* in the asymmetric unit are tabulated since there are differences in the ligand geometries in the two molecules. § There are two conformers of His55 present in the distal cavity, designated *a* and *b*. ¶ Distances from heme iron to CN present in two alternative orientations in the distal pocket, designated CN1 and CN2 (see text). †† Distances of the N atom of CN1 and CN2 to His55*a* are shown. The distances to H55*b* are similar and are discussed in the text. ‡‡ The bend angle is defined as the Fe—C—N angle. §§ The bend angles in subunit *B* of the C73S mutant protein are 123° for CN1 and 163° for CN2. ¶¶ The tilt angle is defined as the angle between the heme perpendicular and the Fe—C bond (Vangberg *et al.*, 1997).

Table 3
Comparison of resolution, completeness and redundancy for various frames of the C73SCN X-ray data set collected using synchrotron radiation.

Values for the completeness and redundancy are obtained from the log files of the respective *SCALEPACK* truncations of the collected data sets.

Group	Frames	Resolution (Å)	Completeness (%)	Redundancy
Total	120	1.31	97.3	4.2
Initial† *A*	60	1.26	92.1	2.3
Initial† *B*	45	1.26	83.5	1.9
Final‡ *A*	60	1.45	74.7	2.6
Final‡ *B*	45	1.45	72.5	1.9

† Initial refers to the first set of 60 (group *A*) or 45 (group *B*) data frames of the total 120 data frames collected that were used to construct electron-density maps. ‡ Final refers to the last set of 60 (group *A*) or 45 (group *B*) data frames of the total 120 frames collected that were used to construct electron-density maps.

crystallographic results. The DHP A crystal structure deposited as PDB entry 2qfk was employed in the computational study. The monomeric form of DHP A was used with a spherical boundary condition. This procedure is justified by the weak contacts between the two monomers (de Serrano *et al.*, 2007; Chen *et al.*, 2009). The bound water in the original metaquo form was replaced by a CN^- ligand. The simulation system was then constructed using the program suite *VMD* (Humphrey *et al.*, 1996). H atoms were added to the protein, which was then solvated with a 26 Å water sphere and charge-balanced with NaCl. The solvated system contained 4900 atoms, of which 1136 were protein atoms. Simulations were carried out using *NAMD* (Phillips *et al.*, 2005) with the modified PARAM27 version of the CHARMM force fields. Spherical boundary conditions were implemented using a constant temperature of 100 K. The constant temperature was maintained using Langevin dynamics with a damping coefficient of 5 ps^{-1}. The initial structure was minimized for 10 000 steps of 0.02 ns and equilibrated in either 1 or 2 ns (5×10^5 or 10^6 steps, respectively) intervals depending on the model system. After each restart the structure was minimized for an additional 5000 steps. Nonbonded interactions were truncated after 12.0 Å and a switching cutoff distance of 10.0 Å for Lennard–Jones parameters was used.

Topology and parameter files were modified to account for both the ferrous and ferric oxidation states of the heme iron, with and without bound ligand, based on density functional theory calculations. Atomic charges and the force constant for free O_2 are provided in the force field supplied by the *NAMD* simulation package.

3. Results

The structures of DHPCN and C73SCN were determined at 100 K at a resolution of 1.26 Å and refined to $R/R_{\rm free}$ factors of 15.7/18.7% and 17.7/19.8%, respectively (Table 1). The main-chain atoms of the two monomers in the asymmetric unit (de Serrano *et al.*, 2007; Chen *et al.*, 2009) superimpose with an r.m.s.d. of 0.448 Å for the wild-type DHP and 0.437 Å for the C73S mutant. Overall, the structure of the DHPCN complex is very similar to the structures of the metaquo DHP and C73S oxy forms, both of which were determined at a resolution of 1.62 Å using a rotating-anode source (de Serrano *et al.*, 2007).

We have observed that ferric metaquo DHP is prone to reduction in the X-ray beam during data collection even using a rotating copper-anode source (de Serrano *et al.*, 2007). Because the samples were prepared in the cyanide-bound form and cooled to 100 K, we assumed that the electron density at the shortest times of observation can be accounted for by CN^-. However, it is not clear that the electron density observed at the first possible observation time in the X-ray beam corresponds to CN^-. Based on the $2F_o - F_c$ maps, both the DHPCN and C73SCN display electron density that can accommodate two distinct conformations of a diatomic ligand: one bound and one at a nonbonding distance from iron. In the first site, designated CN1, the diatomic ligand is coordinated to the heme iron with a distance from iron to the C atom of CN^- of 2.08 Å in the wild-type protein and 2.16 Å in the C73S mutant protein (Table 2). In this first site, CN1, the diatomic ligand has a bent conformation, with an Fe—*X*—*Y* angle of 126° (124° in subunit *B*) in the wild-type DHP adduct. In the C73SCN adduct the angle is 117° (123° in subunit *B*). The second conformation, CN2, is observed at a site about 3.0 Å from the heme iron in a conformation nearly perpendicular to the heme plane. The structure obtained using a rotating-anode source has Fe—C—N angles of 154° and 127° in subunits *A* and *B*, respectively. Hence, the Fe—*X*—*Y* (or Fe—C—N) bond angle in CN1 is not consistent with the perpendicular

geometry expected for a CN^- adduct with ferric heme in any of the structures. Moreover, the appearance of the electron density above the heme iron strongly resembles the C73S structure (PDB code 2qfn; not shown). In the C73S structure the heme was initially in the metaquo form (de Serrano *et al.*, 2007), but is observed to bind O_2 following photoreduction. Comparison of the two structures suggests that photoreduction of Fe^{III} to Fe^{II} by the X-ray beam followed by dissociation of CN^- may have occurred in the structures presented here.

In order to assess the photoreduction phenomenon and the dose-dependence of the electron density in the distal pocket, we analyzed the data sets obtained using synchrotron radiation as the data acquisition progressed. The collected data sets comprising 120 diffraction images (collected at 1° oscillation range) were separated and processed in the groups shown in Table 3. Fig. 2 shows an OMIT map for the ligand to the heme iron for the first and last sets of 60 images acquired from the C73S crystal. The electron density in the distal position, CN2, which is about 3 Å from the heme Fe, is observed to increase as X-ray data collection progresses (Bellelli *et al.*, 1990). Based on a comparison of these changes with the C73S–O_2 structure (PDB code 2qfn), we contemplated the possibility that the electron density arises from CN^-, HCN or O_2 or from a progressive replacement of CN^- by either HCN or O_2. We include HCN in our consideration since protonation of CN^- is possible in the distal pocket following dissociation given that the pK_a of HCN is ∼9.2 and the crystal buffer is at pH 6.5. It is difficult to assess the meaning of pH in a crystal at 100 K, but we consider the possibility that proton transfer occurs to dissociated CN^- to yield HCN.

Regardless of the identity of the diatomic ligand, the electron density in this site may be regarded as a trapped state, which can be compared with the B state of photolyzed Mb*CO (Schlichting *et al.*, 1994; Teng *et al.*, 1994; Srajer *et al.*, 1996; Hartmann *et al.*, 1996; Schotte *et al.*, 2003). The B state for photodissociated CO has been extensively studied by cryogenic and time-resolved X-ray crystallography. However, the conformation of the CN2 molecule is clearly not the same as that of CO in the B state of Mb*CO. Fig. 3 indicates that the diatomic molecule in CN2 is stabilized by hydrogen bonding to the $N^{\varepsilon 2}$ atom of His55 (see Table 2). In contrast, CO in the B state is more nearly parallel to the heme plane. Fig. 3(*a*) shows the structure of PDB entry 3kun (nominally metcyano DHP A) compared with 2qfn (nominally metaquo DHP A; de Serrano *et al.*, 2007). Although CN1 and CN2 are indicated in Fig. 3(*a*), the point of our study is to determine the identity of the molecules that occupy this electron density. A similar electron density can be obtained starting from the metaquo form of the C73S mutant of DHP A. In this structure (2qfn) we assigned the electron density to a diatomic oxygen molecule, which replaced water during the course of X-ray data collection. Fig. 4 shows that a different electron density can be obtained starting from the metcyano form by collecting data

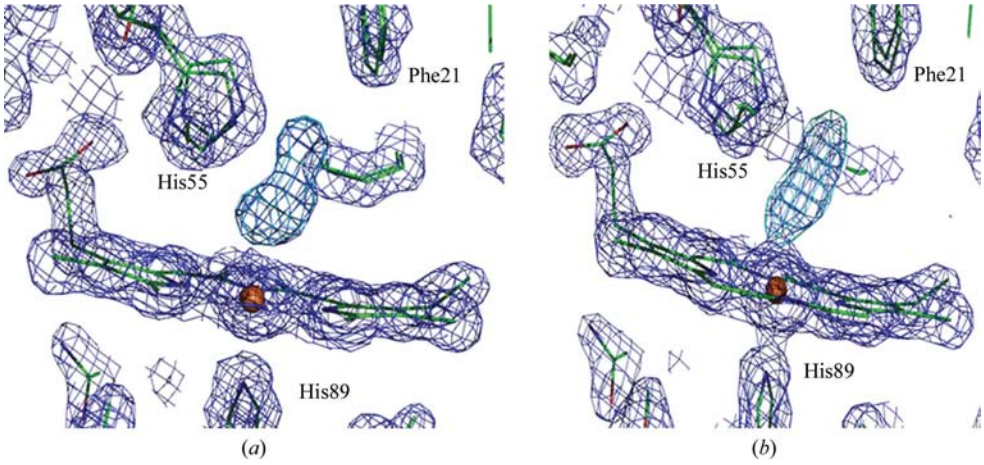

Figure 2
Changes in the ligand electron density during the course of X-ray exposure. The CN^- complex structure is shown for the distal side of the C73S mutant. Electron-density maps, calculated with the ligand omitted, are computed from (*a*) the first 60 and (*b*) the last 60 of the total of 120 collected diffraction images ($2F_o - F_c$ maps contoured at 1.2σ, $F_o - F_c$ maps contoured at 4σ).

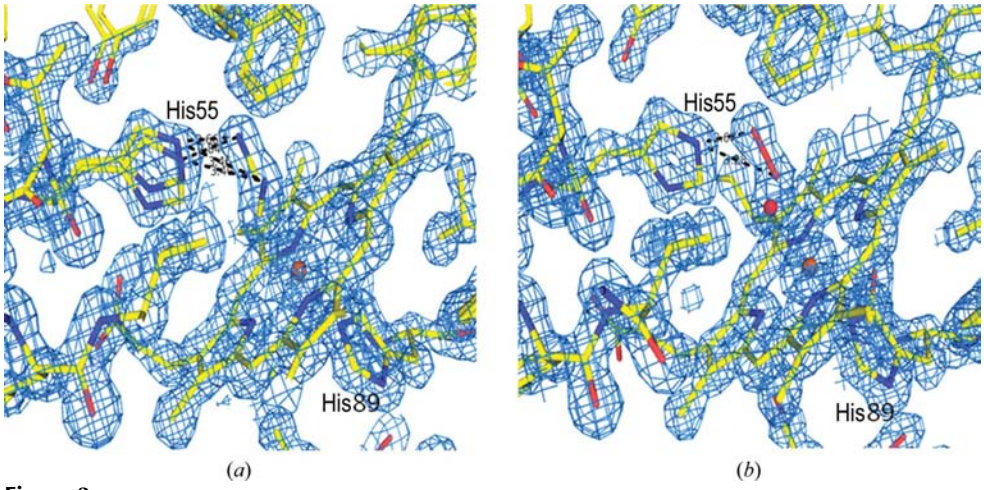

Figure 3
Electron-density maps ($2F_o - F_c$), from data collected on the 22-BM beamline, of wild-type DHP A in complex with cyanide (*a*) and metaquo wild-type protein (*b*). The maps are contoured at the 1.2σ level. The hydrogen bonding of cyanide in two discrete positions with His55 conformers is indicated in the maps, as is the hydrogen bonding of the oxygen molecule and His55 in the wild-type unligated structure. In the distal pocket of the metaquo structure a water molecule and an alternate oxygen molecule are colored red.

Table 4
Comparison of experimental and simulation distances.

	CN ligand (wild type)†	CN ligand (HSD‡)	O_2 ligand (HSD‡)	O_2 ligand (HSE‡)	HCN ligand (HSD‡)
Fe—His89 $N^{\varepsilon 2}$ (Å)	2.16	1.65	1.96	1.96	1.59
Fe—His55*a* $N^{\varepsilon 2}$ (Å)	5.03	6.40	n/a§	n/a§	n/a§
Fe—His55*b* $N^{\varepsilon 2}$ (Å)	5.38	6.60	5.70	5.00	6.38
Fe–ligand (CN1) (Å)	2.08	1.89	2.08	2.08	n/a
Fe–ligand (CN2) (Å)	3.12	10.5	3.76	4.20/6.50¶	4.80
Ligand–His55 (Å)					
CN1 N–H55*a* $N^{\varepsilon 2}$	3.39	4.40	4.33	4.33	n/a
CN2 N–His55*a* $N^{\varepsilon 2}$	2.85	>4.50††	3.29	3.50/4.50	4.40
Fe–ligand bend angle (°)					
CN1	126.2	179.5	124.8	124.8	n/a
CN2	173.3	n/a††	90.0	90.0/130.0¶	153.8

† Experimental distances tabulated for chain *A* of the wild-type DHPCN data set. ‡ HSD refers to the His55 tautomer protonated at the δ-nitrogen; HSE refers to the His55 tautomer protonated at the ε-nitrogen. § No evidence of a second His55 conformation. ¶ Distance of the second occupation site for the O_2 HSE simulation. †† Simulations suggest immediate exit of the CN ligand.

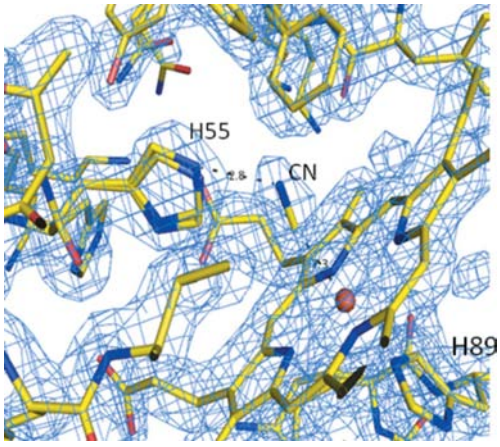

Figure 4
Electron-density maps ($2F_o - F_c$), from data collected using the in-house X-ray generator, of wild-type DHP A in complex with cyanide. The maps are contoured at the 1.2σ level as in Fig. 3. The CN molecule is not coordinated to the heme Fe, but is observed at a distance of 2.3 Å.

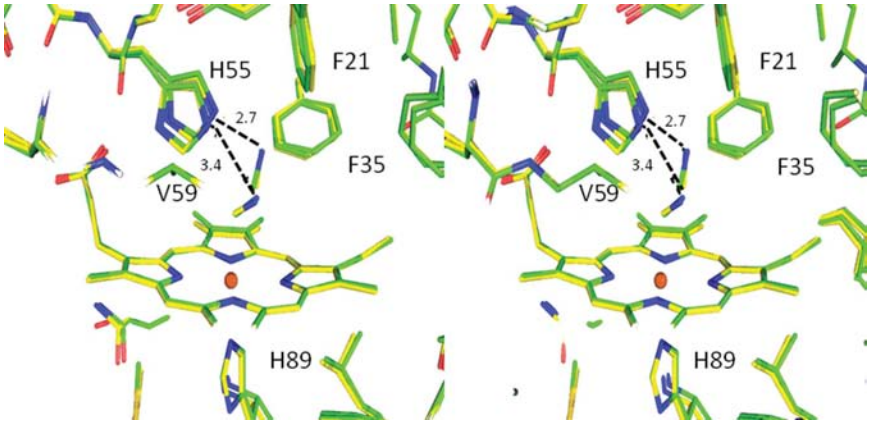

Figure 5
Structural features of the binding of cyanide to the ferric form of DHP. The overlay of the distal sites of wild-type (green) and C73S mutant (yellow) DHP is shown and marker residues of the pocket are labeled. The hydrogen bonding of cyanide to conformers of distal histidine in the wild-type structure is also shown (dashed lines).

at lower X-ray flux and dose using an in-house copper rotating-anode source. The excess density in the 3kun and 3kuo structures may arise from dissociated CN^-, O_2 replacement or some amount of H_2O that associates with these diatomic ligands in the distal pocket. DFT calculated and MD simulations were conducted to obtain models that were consistent with the observed electron density (see below).

3.1. Heme conformation in the DHPCN structure

The conformations of the heme in the DHPCN structures presented here are similar to that in the C73S–O_2 structure, which is consistent with the idea that C73S–O_2 was also formed by photoreduction of the heme iron by synchrotron radiation. The structure of the heme shows relatively minor structural changes in the various frames studied. In both structures there is a heme rotation of 3.6° about the α,γ *meso*-carbon axis. This rotation also helps to position the propionates closer to the positive charge of Lys51. The displacements of iron from the heme pyrrole plane are 0.05 Å in the DHPCN and C73SCN structures and 0.04 Å in the metaquo DHP adduct (Table 2; de Serrano *et al.*, 2007).

3.2. Conformation of the distal histidine His55

In previous work, we established that His55 is present in two orientations, called internal and external. The internal orientation with His55 in the distal pocket is observed in the metaquo and oxyferrous (C73S–O_2) six-coordinate DHP structures (2qfk and 2qfn, respectively). The solvent-exposed or external orientation is observed in the five-coordinate deoxy form (PDB code 3dr9; de Serrano *et al.*, 2007; Chen *et al.*, 2009). The presence of two orientations of the distal histidine has also been observed in high-resolution structures of myoglobin (Vojtechovsky *et al.*, 1999). The flexibility of His55 was also noted in the room-temperature DHP A met(aquo) structure, where there is an equilibrium between the internal and external orientations of this critical residue (LaCount *et al.*, 2000). In the 3kun and 3kuo structures presented in Figs. 3(*a*) and 4, respectively, there are two His55 conformers that are both observed in the internal orientation such that their $N^{\varepsilon 2}$ atom is located close to the bound ligand and their $N^{\delta 1}$ atom is pointing outwards into the solvent. The $N^{\varepsilon 2}$ atom is located at a distance of 5.03 and 5.38 Å from the heme iron in subunits *A* and *B*, respectively, as shown in Table 2. The two conformations most closely resemble the His55 conforma-

Table 5
Potential energies (kJ mol^{-1}) of binding for both ferrous and ferric FeP–CN.

FeP–CN is the Fe porphine model in complex with CN ligand used in geometry optimization and in simulations. LS denotes the low-spin state of the heme iron, whereas HS refers to the high-spin state of the heme iron.

	Q_p = 0.0		Q_p = 0.2		Q_p = 0.4	
	LS	HS	LS	HS	LS	HS
Fe^{II}	−197.5	−74.7	−155.9	−34.7	−91.5	0
Fe^{III}	−282.5	−106.4	−241.2	−69.1	−188.1	−34.7

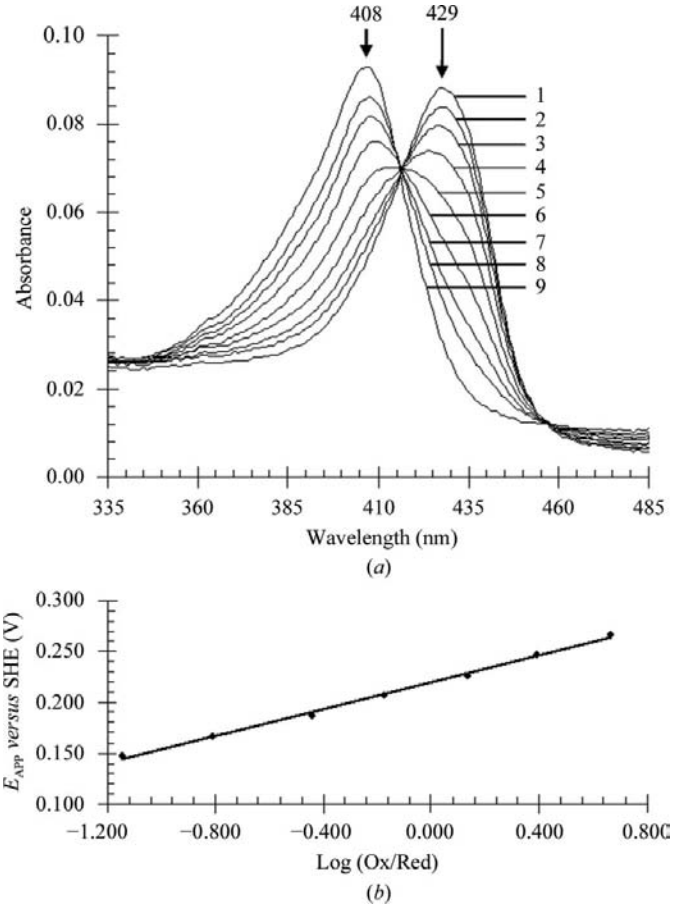

Figure 6
(*a*) UV–visible thin-layer spectroelectrochemical plot for C73S-DHP A in 100 m*M* potassium phosphate buffer pH 7.0; the mediators were $[Ru(en)_3]^{2+}$ and TMPD. Applied potentials (E_{APP} *versus* SHE): (1) −0.103, (2) +0.147, (3) +0.167, (4) +0.187, (5) +0.207, (6) +0.227, (7) +0.247, (8) +0.267 and (9) +0.497 V. (*b*) The Nernst plot for C73S-DHP A.

tions in the C73S–O_2 structure (de Serrano *et al.*, 2007), which are also internal owing to the hydrogen-bonding interaction with the O_2 coordinated to the heme iron. A second conformation is observed for a number of other residues within the distal pocket, which is consistent with the existence of two ligand conformations. This may also in part be a consequence of the higher resolution of this structure compared with previous structures (LaCount *et al.*, 2000; de Serrano *et al.*, 2007). The hydrogen bonding of each of the His55 conformers to the CN1 and CN2 diatomic ligands is shown in Fig. 5.

3.3. Determination of the CN^- dissociation constant of the Fe^{III} and Fe^{II} forms

The photoreduction of Fe^{III} to Fe^{II} leads to a reduced affinity for CN^- binding. We determined the dissociation constant K_d for the binding of CN^- to DHP in the Fe^{III} and Fe^{II} forms by titrating the corresponding protein solution with KCN solution and showed that the Fe^{III} protein form has a much higher affinity for CN^- than the Fe^{II} protein. The K_d values are 6.3×10^{-6} and 0.43 *M* for Fe^{III} and Fe^{II}, respectively, at pH 6.5. This property of DHP compares very closely with that of myoglobin, which has a K_d of 4.4×10^{-6} *M* for the Fe^{III} form at pH 6.6 and 0.4 *M* at pH 9.3 for the Fe^{II} form of the protein (Cox & Hollaway, 1977; Bellelli *et al.*, 1990).

3.4. Determination of the formal reduction potential

Spectroelectrochemical data for the C73S mutation of DHP are shown in Fig. 6. The Soret bands of the metaquo and deoxy forms are observed at 406 and 430 nm, respectively. Similar spectra were obtained for wild-type DHP (D'Antonio *et al.*, 2010). The clear isosbestic point indicates that there are two species present during the experiment: the Fe^{III} and Fe^{II} forms. The solution formal reduction potential of the Fe^{III}/Fe^{II} couple is +0.214 ± 0.006 V *versus* SHE for C73S-DHP A. In comparison, we determined that the reduction potential of horse heart myoglobin was +0.042 ± 0.006 V, which agrees well with the values determined elsewhere (D'Antonio *et al.*, 2010; Heineman *et al.*, 1979).

3.5. DFT calculations of heme structure and potential energy surfaces

DFT geometry optimization of an Fe porphine (FeP) model with axial imidazole (Im) and CN^- or O_2 ligands provides a structure that can be compared with the observed geometry. Geometry-optimized low-spin FeP–CN and FeP–O_2 exhibit angles of 180° and 125°, respectively (Fig. 7). These angles can be compared with the experimental extremes of 154.0° and 126.5° for CN1 and CN2 (Table 4). For DHP, the Fe—O—O angle is 144° (PDB code 2qfn; de Serrano *et al.*, 2007) and for MbO_2 the Fe—O—O angle is 123° (PDC code 1a6m; Vojtechovsky *et al.*, 1999). The calculated Fe—C and Fe—O bond lengths are 1.89 and 2.08 Å (Table 4), respectively, compared with an observed Fe–ligand distance of 2.08 Å for CN1 (Table 2).

Fig. 8 shows the potential energy surfaces for FeP–CN in both the ferric and ferrous oxidation states. Surfaces were calculated for both low-spin (S = 1/2 and S = 0) and high-spin (S = 5/2 and S = 2) configurations for Fe^{III} and Fe^{II} oxidation states, respectively. The calculations were carried out at three values of Q_p, a coordinate that represents the iron out-of-plane distance relative to the plane of the pyrrole N atoms of the heme. For Q_p = 0.0 Å, where the iron is entirely in plane with the heme, the binding energies are −197.5 and

−282.5 kJ mol^{-1} for low-spin Fe^{II} and Fe^{III}. As the iron changes from a low-spin state to a high-spin state, the Fe—CN binding energy decreases for the ferric and ferrous oxidation states by 176 and 123 kJ mol^{-1}, respectively. As the iron is displaced out of the heme plane, *i.e.* as Q_p increases, there is a decrease in the Fe—CN binding energy of ∼35 kJ mol^{-1} for a corresponding increase in Q_p of 0.2 Å. High-spin ferrous iron with a heme displacement of 0.4 Å corresponds to the geometry of deoxy heme. This has been found to be a dissociative state (Franzen, 2002). All others surfaces correspond to bound states. Table 5 gives a summary of the calculated binding energies, which are in agreement with the dissociation constants determined experimentally, as discussed above.

3.6. Molecular-dynamics trajectories for models of coordination ligands

MD simulations were carried out to further clarify the identity of the diatomic ligand in the distal pocket after X-ray-induced reduction of Fe^{III} to Fe^{II}. Simulations were performed on three ligands: free O_2, HCN and CN^-. In addition, in order to further examine the identity of the ligand, O_2 simulations were carried out for the δ- and ε-tautomers of His55, where the N$^{\delta}$—H and N$^{\varepsilon}$—H tautomers are named HSD and HSE, respectively. In all simulations, the heme Fe was in the ferrous oxidation state and the simulations were carried out using the same force field, with the exception of the force-field terms that apply to the diatomic ligand. The major difference in the simulations is the charge on the ligand, since CN^- carries a charge of −1 and HCN and O_2 are both neutral molecules. In the DHPCN simulation the overall neutrality of the system was satisfied by

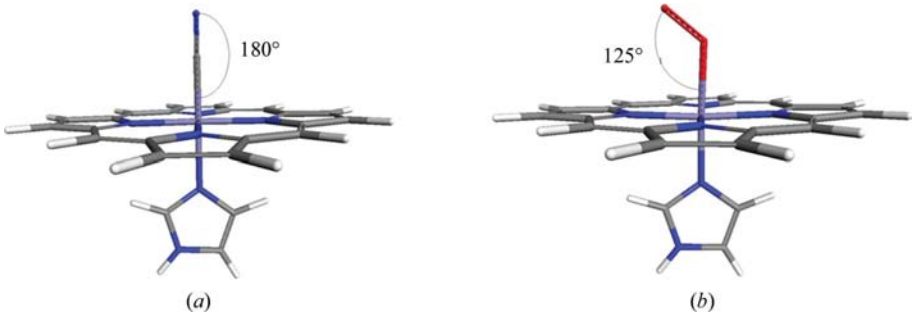

Figure 7
Optimized geometry of the ferric form of heme displaying the bond angle for (*a*) Fe^{III}P–CN and (*b*) Fe^{III}P–O_2. The DFT method was used for the iron-porphine model of the heme as described in the text.

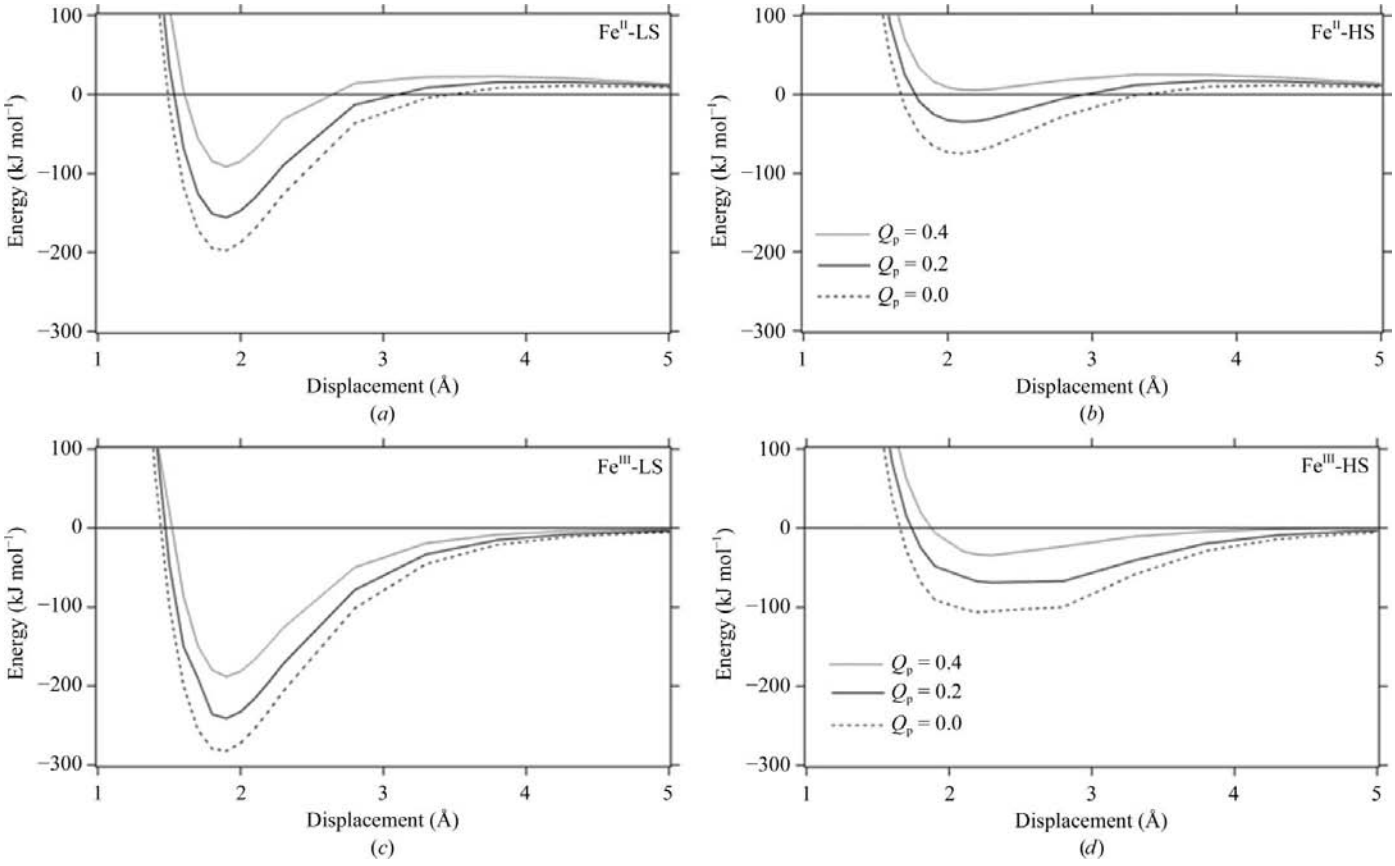

Figure 8
Calculated potential energy surfaces for FeP–CN. (*a*) Surface for ferrous iron, low spin. (*b*) Surface for ferrous iron, high spin. (*c*) Surface for ferric iron, low spin. (*d*) Surface for ferric iron, high spin. Q_p denotes the iron distance from the heme plane.

introducing one Na^+ ion into the water sphere surrounding the protein. The CN^- starting geometry was normal to the heme plane and the N atom is observed at distances of 2.8 and 3.5 Å from the N^{ε} atoms of His55 and Fe, respectively. In O_2 simulations, both tautomeric forms started with the free ligand in the same position: normal to the heme plane. The distal O atom is positioned 2.8 and 3.5 Å away from N^{ε} and Fe, respectively. HCN was also positioned normal to the heme plane, with the N atom at distances of 3.2 and 1.8 Å from His55 N^{ε} and Fe, respectively. In all cases, the His55 starting conformation was closed (inside the distal pocket).

3.7. CN^- ligand

Simulations involving the CN^- ligand were carried out for 4.30 ns. At the start of the simulation, the Fe–CN iron–nitrogen distance was 3.5 Å. Within 0.02 ns of the start of the simulation, the CN^- ligand migrates out of the distal pocket and into the solvation sphere. The iron–nitrogen distance increases to 8.0 Å (by approximately 4.5 Å) and then further to 10 Å for the remainder of the simulation (data not shown). This behavior is attributed to electrostatic interactions between the negatively charged CN^- ligand and the amino acids that make up the distal cavity. At the start of the simulation the distance between His55 N^{ε} and CN^- is 3.8 Å and it increases to 4.4 Å as CN^- exits the pocket and enters the solvation sphere. As the ligand starts to migrate out of the pocket and approaches His55, this amino acid can be seen to move to a more solvent-exposed position. Originally 6.4 Å, the Fe—N^{ε} distance increases by 0.2 Å as ligand migration begins, while the dihedral angle between the imidazole and the backbone of His55 changes by 30° (from 105° to 75°). Owing to this concerted motion between His55 and CN^-, the distance between the ligand and N^{ε} remained constant at 4.5 Å throughout the remainder of the simulation.

3.8. O_2 ligand

Simulations involving the O_2 ligand for both tautomers of His55 were performed for 8.0 ns; longer times were used than the CN^- simulation times owing to the observation that the O_2 ligand remains within the distal pocket. A shorter simulation time was possible for CN^- since it was observed to rapidly exit the pocket.

3.8.1. HSD tautomer. For the full 8.0 ns, O_2 remains stationary within the distal pocket. The O_2 molecule rests parallel to the heme plane at a distance of 3.8 Å from the heme iron, maintaining a constant iron–ligand (Fe—O_2) bend angle of ∼90°. For bound ligand (state CN1) the distance to His55, O_2—N^{ε}, was 4.3 Å and for the free ligand (state CN2) this distance decreased to 3.3 Å. This difference is not a result of the two His55 conformations shown in Fig. 3(*a*). Rather, the effect arises from the ability of the unbound diatomic ligand to position itself at a close hydrogen-bonding distance to His55. Fluctuations of 0.20 Å were observed in the N^{ε}—O1 distance throughout the 8.0 ns for O_2 in the CN2 state and were attributed to the rotation of the free ligand above the heme plane. The Fe—N^{ε} distance remained constant at a distance of 5.7 Å for the duration of the simulation.

3.8.2. HSE tautomer. Similar to the HSD simulation, O_2 remains inside in the distal pocket for the full 8.0 ns of simulation time. However, O_2 occupies two different sites within the pocket in the HSE simulation. Initially 4.2 Å, the Fe—O_2 distance increases to 6.5 Å within 0.2 ns (Fig. 9*a*). The O_2—N^{ε} distance fluctuates between 3.5 and 4.5 Å when O_2 moves from site 1 to site 2. His55 is positioned more deeply in the distal pocket in the HSE tautomer than in the HSD tautomer. A difference of 0.7 Å is observed between the two Fe—N^{ε} distances, with the protonated N^{ε} of HSE at 5.0 Å and the unprotonated N^{ε} being positioned 5.7 Å away from the heme Fe. In addition, the Fe—O_2 bend angle varies randomly between 90° and 130° during the course of ligand migration throughout the 8.0 ns simulation run.

3.9. HCN ligand

We also investigated the possibility that the observed electron density in the crystal structure corresponded to HCN. As with O_2, HCN remained inside the distal pocket throughout 8.0 ns of simulation time. Simulation results show that HCN hydrogen bonds to the heme iron and remains

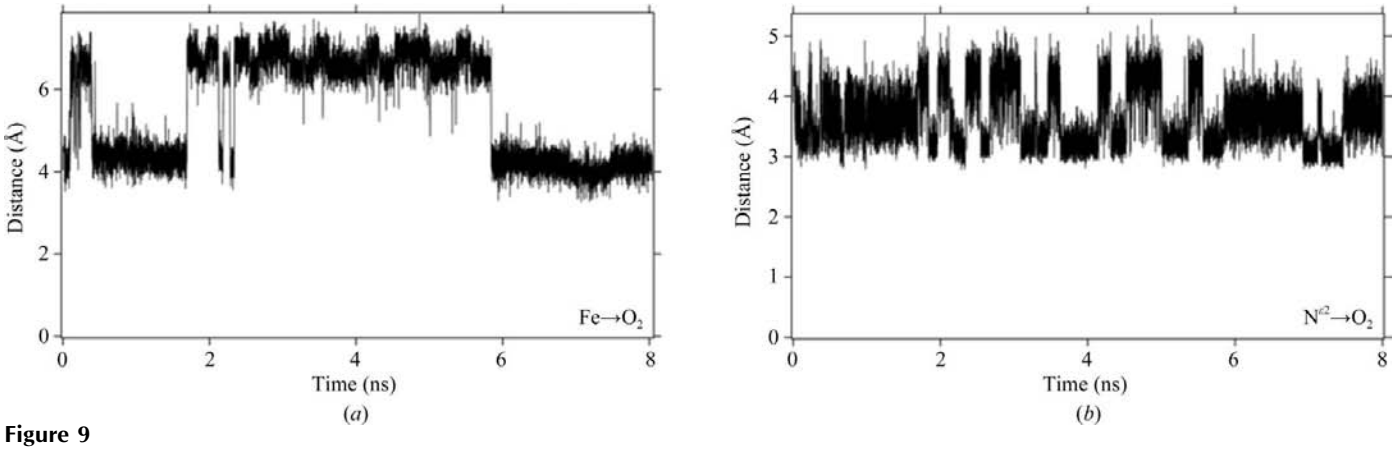

Figure 9
Distance *versus* time for the O_2 HSE simulation results. The arrow depicts the distance being measured. (*a*) Iron–O_2 ligand distance for the HSD tautomer. (*b*) O_2—His55 N^{ε} distance. Both distances are represented as an arrow between iron and the ligand at the bottom of the figure. The migration of the ligand within the distal pocket is depicted by the fluctuations in distance for the respective measurement.

stationary above the heme plane with no change in orientation. As a result, the iron–ligand distance is reported as the Fe—C distance (the C atom in this instance being oriented away from the iron), not the Fe—N distance as was performed in the CN^- simulation. This distance remained constant at 3.8 Å. The Fe—N^{ε} distance and Fe–ligand bend angle also remained constant at 6.4 Å and 154°, respectively.

4. Discussion

The presence of two alternate conformations of a diatomic ligand in the distal pocket of heme is attributed to photoreduction of Fe^{III}–CN to Fe^{II}–CN followed by dissociation of the Fe^{II}—CN bond. We have investigated this hypothesis by measurement of the CN^--dissociation constant for the Fe^{III} and Fe^{II} forms of DHPCN, measurement of the formal reduction potential, DFT and MD calculations. These studies are relevant for X-ray crystallographic studies of ferric heme proteins in general where photoreduction is an inherent side-effect of data collection, particularly using synchrotron radiation. DHP A is an interesting case because its reduction potential is the highest known for any Hb (with the exception of the giant Hb of *Lumbricus*; Harrington *et al.*, 2007) and thus it is more prone to photoreduction. The functional significance of the higher redox potential is still not clear, but it may provide a means for DHP A to cycle between two functions by favoring reduction of the heme iron under conditions where H_2O_2 is not present. Thus, it is possible that the dual function of DHP A is maintained by the local environment in the coelom of *A. ornata*. The C73S mutant has a 0.012 V higher reduction potential than wild-type DHP A, which is consistent with the observation that photoreduction is more facile in the C73S mutant than in wild-type DHP A. Cys73 is a surface cysteine that is located near the dimer interface in the X-ray crystal structure (PDB code 2qfn). The mutation C73S has no major effect on protein structure, but may play a role in protein–protein interactions in solution. The functional consequence of the high reduction potential of DHP A remains to be explained since it is nearly 0.5 V more positive than that of HRP (Battistuzzi *et al.*, 2002). This fact suggests that activation of H_2O_2 (or possibly O_2) in DHP A occurs by a different mechanism from that in typical peroxidases.

Photoreduction can lead to dissociation provided that there is a change in the ligation strength that depends on the oxidation state of the heme iron. Equilibrium binding studies of CN^- provide a means to test the relative stability of the Fe^{II}–CN and Fe^{III}–CN adducts. The experimentally observed difference in binding constant corresponds to a loss in stabilization free energy of the Fe–CN adduct of 27.3 kJ mol^{-1} upon reduction from Fe^{III} to Fe^{II}. Consistent with this loss of stabilization, spectroscopic studies of the dithionite reduction of the Fe^{III}–CN adduct of myoglobin (MbCN) provide evidence for the transient formation of an unstable Fe^{II} MbCN intermediate in the process of forming the final product, deoxy Mb (Cox & Hollaway, 1977; Bellelli *et al.*, 1990). Ligand destabilization upon chemical reduction was not observed for the metMb adducts of other ligands such as SCN^-, N_3^- and F^-. These observations support the hypothesis that photoreduction will destabilize CN^- coordination to the heme iron.

While the data are consistent with facile photoreduction in DHP A, it is more difficult to discern the identity of the molecule that occupies the extra electron density in the distal pocket of DHP A shown in Figs. 2 and 3, which is associated with an apparent second conformation of a diatomic ligand. The evolution of the geometry of the DHPCN structure can be explained by the dissociation and migration of the CN^- ligand. We consider below the possibility that the identity of the diatomic ligand changes during the course of X-ray data collection. However, first we consider the evidence that the change in the Fe—C—N angle over time is the result of CN^- dissociation. Since CN^- is isoelectronic with CO, the Fe—C—N angle in FeP–CN should be similar to the angle of 179° found for Fe—C—O in MbCO (Lim *et al.*, 1995) and as observed in model porphyrin–CO complexes (Peng & Ibers, 1976). Early studies of MbCN suggested that the Fe—C—N is nearly linear (Deatherage *et al.*, 1976) but slightly tilted from the heme normal. High-resolution X-ray diffraction and XANES structural studies agree that the Fe—C—N angle is 166–170° in MbCN (PDB codes 1ebc and 2jho; Bolognesi *et al.*, 1999; Arcovito *et al.*, 2007). However, at room temperature photoreduction and photolysis was observed that gave rise to an Fe—C—N angle of approximately 90°, as observed in photolyzed Fe-CO (Schlichting *et al.*, 1994; Teng *et al.*, 1994; Hartmann *et al.*, 1996; Srajer *et al.*, 1996; Schotte *et al.*, 2004). Consistent with these precedents, the Fe—C—N angle observed in the DHPCN structure has a maximum value of ∼154° and decreases progressively thoughout data collection to a value of ∼126°. Our interpretation of the fact that the largest angle is 154°, rather than the 170° found in the 1ebc or 2jho structures, is that Fe^{III} is reduced so readily in the DHPCN structure that some amount of Fe reduction has occurred even in the shortest possible time frames in our data collection, which is best modeled by a single CN^- displaced from the linear conformation.

The fate of the dissociated CN^- ligand could be either to remain in the distal pocket and possibly to be protonated to form HCN or to escape and be replaced by O_2. The phenomenon of reduction of the heme iron center and concomitant dissociation of CN^- is reminiscent of the phenomenon of photolysis of carbon monoxide from the MbCO complex and subsequent entrapment of CO in the 'Xe' binding sites (Schlichting *et al.*, 1994; Teng *et al.*, 1994; Hartmann *et al.*, 1996; Srajer *et al.*, 1996; Schotte *et al.*, 2004). However, the negative charge on CN^- may have an effect on the conformation assumed in the distal pocket and possibly on the escape trajectory. In the C73S mutant metaquo structure (PDB code 2qfn), Fe^{III}–OH_2 was replaced by Fe^{II}–O_2 during the course of data collection as a result of reduction of the heme iron center (de Serrano *et al.*, 2007). The OMIT-map electron density in the C73S–O_2 structure is similar to the apparent OMIT-map electron density in the C73SCN and DHPCN structures, leading to the suggestion that O_2 is able to diffuse into the distal pocket and replace CN^- under the conditions of both experiments.

Given the difficulty in identifying the diatomic ligand in the X-ray crystal structures, we employed DFT calculations of the ImFeP–CN and ImFeP–O_2 structures and MD simulations of the respective ligand trajectories to provide support for the model that O_2 replaces CN^- during data collection. Firstly, geometry optimizations of $ImFe^{III}$–CN and $ImFe^{II}$–O_2 suggest that the electron density observed in the CN1 state is that of O_2. The reported Fe–CN bend angle is 126°. Calculations show that this bend angle does not agree with the calculated Fe^{III}–CN bend angle of 180°, but corresponds to bound O_2 with a calculated angle of 125° (Table 4). The experimental Fe–ligand bond length is 2.1 Å, corresponding to the calculated Fe—O bond length of 2.08 Å, not the Fe—C bond length of 1.89 Å. However, XANES provides evidence for a significantly shorter Fe—CN bond (Arcovito *et al.*, 2007) so that the comparison of bond lengths is only valid in a relative sense. Secondly, potential energy surfaces were generated to study the binding energies of FeP–CN for various spin and oxidation states. Taking into account all possible spin states and out-of-plane conformations (spin $S = 0$ and 2 for Fe^{II} or $S = 1/2$ and 5/2 for Fe^{III} and $Q_p = 0.0$, 0.2 or 0.4 Å), only one dissociative state was observed, high-spin Fe^{II}, in which the iron was displaced 0.4 Å out of the heme plane. DFT results suggest that heme undergoes photoreduction from the ferric to the ferrous form, with a decrease in calculated Fe–CN binding energy of $\Delta E = 85$ kJ mol^{-1}, which may be accompanied by cleavage of the Fe—CN bond when the iron heme experiences a rapid out-of-plane motion. The magnitude of the calculated free-energy change (85 kJ mol^{-1}) is larger than the measured change based on the difference in Fe–CN dissociation constants (27 kJ mol^{-1}); this is most likely to be a consequence of the additional interactions of the diatomic ligand with His55, which were not included in the calculation.

Several molecular-dynamic simulations were performed to further elucidate the identity of the electron density observed in the $2F_o - F_c$ map. As mentioned above, possible candidates for this density included CN^-, HCN and O_2. The results of the MD simulations propose that the observed electron density was neither CN^- nor HCN. The CN^- ligand was observed to immediately exit the distal pocket and migrate into the solvation sphere, which is consistent with loss of CN^- from the distal pocket. The simulations show HCN hydrogen bonding to the heme iron. This orientation is contrary to the observed electron density, which is consistent with two conformations: one that is bound to the iron (not hydrogen bonded) and a second that is stabilized within the pocket by forming a hydrogen bond to His55. Simulations of the DHP–O_2 system yielded the closest agreement with the experimental data. Both tautomeric forms of His55 (HSD and HSE) were studied in order to obtain a more precise model of the conformation of O_2. The HSD results exhibited the best agreement with the experimental distances (all within 1.0 Å). However, the HSE tautomer showed the closest agreement with the Fe-O_2 bend angle for dissociated O_2, *i.e.* the CN2 conformation. The experimental Fe—O—O angle for CN2 is 173°, while the calculated angle is 90° and 130° for the HSD and HSE tautomers, respectively. Moreover, the O_2 ligand moves from ~4 to ~7 Å in the HSE simulation, which corresponds to migration into the Xe4 binding site (Nienhaus *et al.*, 2006). We have recently confirmed by X-ray crystallography that a similar Xe-binding site also exists in DHP A (de Serrano *et al.*, manuscript in preparation). In summary, it appears that some combination of the HSD and HSE simulations gives agreement with the experimental electron density if O_2 is the ligand.

5. Conclusions

We have observed photoreduction of the ferric heme iron from Fe^{III} to Fe^{II}, which appears to lead to dissociation of CN^- originally bound to the heme iron. The photoreduction depends on the duration of exposure to X-ray radiation. The ease of photoreduction is consistent with the high reduction potential of the heme Fe in DHP A relative to other Hbs. The reduction potential is completely outside the normal range for peroxidases, suggesting that DHP A may activate H_2O_2, or even O_2, by a different mechanism, such as electron transfer from an as yet unidentified cofactor. The OMIT-map electron density, dissociation constant and potential energy surfaces calculated by DFT methods are consistent with dissociation of CN^- from Fe^{II}. MD simulations provide evidence for the replacement of CN^- by O_2 in the distal cavity at 100 K. Based on the comparison of MD trajectories with the structure, His55 appears to play a role in stabilizing O_2 in the distal pocket by hydrogen-bond formation. The ease of ligand substitution in the distal pocket is consistent with our previous X-ray crystal structures (PDB codes 3dr9 and 2qfk), which show that His55 is unusually flexible in DHP A. The significant role played by hydrogen bonding of His55 to O_2 further supports the proposed role of His55 as an acid–base catalyst in the heterolytic cleavage of hydrogen peroxide and removal of the generated water molecule, which are both essential elements of the peroxidase mechanism.

We would like to thank Gerald Guanga and Dr Greg Buhrman of the Department of Molecular and Structural Biochemistry at North Carolina State University for collecting data on the SER-CAT synchrotron beamline at the Advanced Photon Source in Argonne, Illinois. Use of the Advanced Photon Source was supported by the US Department of Energy, Office of Science, Office of Basic Energy Sciences under Contract No. W-31-109-Eng-38. SF and EFB acknowledge support from the Army Research Office through grants 52278-LS and 51432-CH-SR, respectively.

References

Arcovito, A., Benfatto, M., Cianci, M., Hasnain, S. S., Nienhaus, K., Nienhaus, U., Savino, C., Strange, R. W., Vallone, B. & Della Longa, S. (2007). *Proc. Natl Acad. Sci. USA*, **104**, 6211–6216.

Battistuzzi, G., Borsari, M., Ranieri, A. & Sola, M. (2002). *J. Am. Chem. Soc.* **124**, 26–27.

Becke, A. D. (1988). *Phys. Rev. A*, **38**, 3098–3100.

Bellelli, A., Antonini, G., Brunori, M., Springer, B. A. & Sligar, S. G. (1990). *J. Biol. Chem.* **265**, 18898–18901.

Belyea, J., Belyea, C. M., Lappi, S. E. & Franzen, S. (2006). *Biochemistry*, **45**, 14275–14284.

Belyea, J., Gilvey, L. B., Davis, M. F., Godek, M., Sit, T. L., Lommel, S. A. & Franzen, S. (2005). *Biochemistry*, **44**, 15637–15644.

Blair-Johnson, M., Fiedler, T. & Fenna, R. (2001). *Biochemistry*, **40**, 13990–13997.

Bolognesi, M., Rosano, C., Losso, R., Borassi, A., Rizzi, M., Wittenberg, J. B., Boffi, A. & Ascenzi, P. (1999). *Biophys. J.* **77**, 1093–1099.

Brünger, A. T., Adams, P. D., Clore, G. M., DeLano, W. L., Gros, P., Grosse-Kunstleve, R. W., Jiang, J.-S., Kuszewski, J., Nilges, M., Pannu, N. S., Read, R. J., Rice, L. M., Simonson, T. & Warren, G. L. (1998). *Acta Cryst.* D**54**, 905–921.

Chance, B. (1943). *J. Biol. Chem.* **179**, 1299–1309.

Chance, B., Angiolillo, P., Yang, E. K. & Powers, L. (1980). *FEBS Lett.* **112**, 178–182.

Chen, Y. P., Woodin, S. A., Lincoln, D. E. & Lovell, C. R. (1996). *J. Biol. Chem.* **271**, 4609–4612.

Chen, Z., de Serrano, V., Betts, L. & Franzen, S. (2009). *Acta Cryst.* D**65**, 34–40.

Collaborative Computational Project, Number 4 (1994). *Acta Cryst.* D**50**, 760–763.

Cox, R. P. & Hollaway, M. R. (1977). *Eur. J. Biochem.* **74**, 575–587.

D'Antonio, E., Bowden, E. & Franzen, S. (2010). Submitted.

Davis, M. F., Gracz, H., Vendeix, F. A. P., de Serrano, V., Somasundaram, A., Decatur, S. M. & Franzen, S. (2009). *Biochemistry*, **48**, 2164–2172.

Deatherage, J. F., Loe, R. S., Anderson, C. M. & Moffat, K. (1976). *J. Mol. Biol.* **104**, 687–706.

DeLano, W. L. (2002). *The PyMOL Molecular Graphics System.* DeLano Scientific, San Carlos, California, USA.

Delley, B. (1990). *J. Chem. Phys.* **92**, 508–517.

Delley, B. (2000). *J. Chem. Phys.* **113**, 7756–7764.

Edwards, S. L. & Poulos, T. L. (1990). *J. Biol. Chem.* **265**, 2588–2595.

Emsley, P. & Cowtan, K. (2004). *Acta Cryst.* D**60**, 2126–2132.

Fedorov, R., Ghosh, D. K. & Schlichting, I. (2003). *Arch. Biochem. Biophys.* **409**, 25–31.

Feducia, J., Dumarieh, R., Gilvey, L. B. G., Smirnova, T., Franzen, S. & Ghiladi, R. A. (2009). *Biochemistry*, **48**, 995–1005.

Franzen, S. (2002). *Proc. Natl Acad. Sci. USA*, **99**, 16754–16759.

Franzen, S., Gilvey, L. B. & Belyea, J. (2007). *Biochim. Biophys. Acta*, **1774**, 121–131.

Fukuyama, K. & Okada, T. (2007). *Acta Cryst.* D**63**, 472–477.

Furtmüller, P. G., Zederbauer, M., Jantschko, W., Helm, J., Bogner, M., Jakopitsch, C. & Obinger, C. (2006). *Arch. Biochem. Biophys.* **445**, 199–213.

George, S. J., Fu, J., Guo, Y., Drury, O. B., Friedrich, S., Rauchfuss, T., Volkers, P. I., Peters, J. C., Scott, V., Brown, S. D., Thomas, C. M., Cramer, S. P. (2008). *Inorg. Chim. Acta*, **361**, 1157–1165.

Han, K. P., Woodin, S. A., Lincoln, D. E., Fielman, K. T. & Ely, B. (2001). *Mar. Biotechnol.* **3**, 287–292.

Harrington, J. P., Kobayashi, S., Dorman, S. C., Zito, S. L. & Hirsh, R. E. (2007). *Artif. Cells Blood Substit. Immobil. Biotechnol.* **35**, 53–67.

Hartmann, H., Zinser, S., Komninos, P., Schneider, R. T., Nienhaus, G. U. & Parak, F. (1996). *Proc. Natl Acad. Sci. USA*, **93**, 7013–7016.

Heineman, W. R., Meckstroth, M. L., Norris, B. J. & Su, C. (1979). *J. Electroanal. Chem.* **104**, 577–585.

Humphrey, W., Dalke, A. & Schulten, K. (1996). *J. Mol. Graph.* **14**, 33–38.

Keilin, D. & Hartree, E. F. (1955). *Biochem. J.* **61**, 153–171.

LaCount, M. W., Zhang, E., Chen, Y. P., Han, K., Whitton, M. M., Lincoln, D. E., Woodin, S. A. & Lebioda, L. (2000). *J. Biol. Chem.* **275**, 18712–18716.

Laskowski, R. A., MacArthur, M. W., Moss, D. S. & Thornton, J. M. (1993). *J. Appl. Cryst.* **26**, 283–291.

Lee, C. T., Yang, W. T. & Parr, R. G. (1988). *Phys. Rev. B*, **37**, 785–789.

Lim, M., Jackson, T. A. & Anfinrud, P. A. (1995). *Science*, **269**, 962–966.

Lincoln, D. E., Fielman, K. T., Marinelli, R. L. & Woodin, S. A. (2005). *Biochem. Syst. Ecol.* **33**, 559–570.

McCoy, A. J., Grosse-Kunstleve, R. W., Storoni, L. C. & Read, R. J. (2005). *Acta Cryst.* D**61**, 458–464.

Murshudov, G. N., Vagin, A. A. & Dodson, E. J. (1997). *Acta Cryst.* D**53**, 240–255.

Murray, J. W., Rudiño-Piñera, E., Owen, R. L., Grininger, M., Ravelli, R. B. G. & Garman, E. F. (2005). *J. Synchrotron Rad.* **12**, 268–275.

Nienhaus, K., Deng, P. C., Belyea, J., Franzen, S. & Nienhaus, G. U. (2006). *J. Phys. Chem. B*, **110**, 13264–13276.

Nienhaus, K., Nickel, E., Davis, M. F., Franzen, S. & Nienhaus, G. U. (2008). *Biochemistry*, **47**, 12985–12994.

Otwinowski, Z. & Minor, W. (1997). *Methods Enzymol.* **276**, 307–326.

Peng, S.-M. & Ibers, J. A. (1976). *J. Am. Chem. Soc.* **98**, 8032–8036.

Phillips, J. C., Braun, R., Wang, W., Gumbart, J., Tajkhorshid, E., Villa, E., Chipot, C., Skeel, R. D., Kale, L. & Schulten, K. (2005). *J. Comput. Chem.* **26**, 1781–1802.

Sanctis, D. de, Ascenzi, P., Bocedi, A., Dewilde, S., Burmester, T., Hankeln, T., Moens, L. & Bolognesi, M. (2006). *Biochemistry*, **45**, 10054–10061.

Schlichting, I., Berendzen, J., Philips, G. N. Jr & Sweet, R. M. (1994). *Nature (London)*, **371**, 808–812.

Schotte, F., Lim, M. H., Jackson, T. A., Smirnov, A. V., Soman, J., Olson, J. S., Phillips, G. N., Wulff, M. & Anfinrud, P. A. (2003). *Science*, **300**, 1944–1947.

Schotte, F., Soman, J., Olson, J. S., Wulff, M. & Anfinrud, P. A. (2004). *J. Struct. Biol.* **147**, 235–246.

Serrano, V. de, Chen, Z., Davis, M. F. & Franzen, S. (2007). *Acta Cryst.* D**63**, 1094–1101.

Serrano, V. de, D'Antonio, J., Thompson, M., Franzen, S. & Ghiladi, R. A. (2010). Submitted.

Smolenaers, P. J. & Beattie, J. K. (1979). *Inorg. Synth.* **19**, 117–121.

Srajer, V., Teng, T.-Y., Ursby, T., Pradervand, C., Ren, Z., Adachi, S.-I., Schildkamp, W., Bourgeois, D., Wulff, M. & Moffat, K. (1996). *Science*, **274**, 1726–1729.

Sugishima, M., Sakamoto, H., Noguchi, M. & Fukuyama, K. (2003). *Biochemistry*, **42**, 9898–9905.

Teng, T.-Y., Srajer, V. & Moffat, K. (1994). *Nature Struct. Biol.* **1**, 701–705.

Thompson, M. K., Davis, M. F., de Serrano, V., Nicoletti, F. P., Howes, B. D., Smulevich, G. & Franzen, S. (2010). In the press.

Vangberg, T., Bocian, D. F. & Ghosh, A. (1997). *J. Biol. Inorg. Chem.* **2**, 526–530.

Vojtechovsky, J., Chu, K., Berendzen, J., Sweet, R. M. & Schlichting, I. (1999). *Biophys. J.* **77**, 2153–2174.

Weinert, M. & Davenport, J. W. (1992). *Phys. Rev. B*, **45**, 13709–13712.